Materials Science and Engineering A 527 (2010) 3757–3763

Contents lists available at ScienceDirect

Materials Science and Engineering A

journal homepage: www.elsevier.com/locate/msea

Structure and mechanical properties of Al–Ni–Ti amorphous powder consolidated by pressure-less, pressure-assisted and spark plasma sintering

Suhrit Mula [a], K. Mondal [b], Sudipto Ghosh [c], Shyamal K. Pabi [c,*]

[a] Metallurgical and Materials Engineering, National Institute of Technology, Rourkela 769008, India
[b] Materials and Metallurgical Engineering, Indian Institute of Technology, Kanpur 208016, India
[c] Metallurgical and Materials Engineering, Indian Institute of Technology, Kharagpur 721302, India

ARTICLE INFO

Article history:
Received 25 March 2009
Received in revised form 2 February 2010
Accepted 18 March 2010

Keywords:
Intermetallics
Spark plasma sintering
Amorphous
Mechanical properties
Electron microscopy

ABSTRACT

Attempts have been made to prepare highly dense bulk Al-based nanocomposite consisting of evenly distributed nano-intermetallic particles and amorphous phase by consolidating mechanically alloyed amorphous $Al_{88}Ni_6Ti_6$ powder using spark plasma sintering (SPS), hot-pressing and pressure-less sintering techniques. SPS technique has been most effective in comparison to other two processes in getting better homogeneity of microstructural features, densification and mechanical properties due to lower sintering temperature and time, hindering excessive crystallization of amorphous phase and grain growth of formed nanocrystals. This helps in producing optimum microstructure consisting of homogeneous distribution of nanocrystalline intermetallic phase and remaining amorphous phase as revealed by detailed electron microscopy and nano-indentation tests.

1. Introduction

The demand of low density and high strength materials in automotive and aerospace industries is ever increasing in order to reduce the fuel consumption [1–4]. There has been a constant effort to increase the strength of Al-based alloys by making nanocomposite with a novel microstructure consisting amorphous and nanocrystalline phases so that it can even replace some of the high strength Ti-based and Fe-based auto and aero components and it can further decrease the weight [5–16]. Either MA followed by consolidation or rapid solidification techniques are used to make such microstructures. Recent reports [17–19] show that even 1.5–2 GPa strength can be obtained from Al-based nanocomposites. However, it is a challenging task to obtain a fully amorphous structure by MA of Al-based alloys containing more than 80 at.% Al and then to consolidate the amorphous powder into a fully dense bulk product having the desired nano-features [20]. Hence, it is difficult to make use of the superior mechanical properties of these alloys for engineering applications [21].

Consolidation of the amorphous/nanocrystalline powder by conventional techniques including cold isostatic pressing followed by extrusion [22] or hot isostatic pressing [23] can lead to excessive crystallization and grain growth resulting inferior mechanical properties of the consolidated bulk samples. Recent studies [24,25] have demonstrated that spark plasma sintering (SPS) is remarkably successful in full consolidation of a nanostructured or amorphous powder into a dense bulk material without excessive grain growth or crystallization in a shorter time and at lower temperatures, as compared to the conventional methods. However, very limited information is available on the use of SPS for sintering low melting alloys such as Al-based alloys, especially Al-rich amorphous alloys.

In the present study, conventional pressure-less sintering, hot-pressing and SPS methods have been employed to consolidate a recently developed [26,27] mechanically alloyed Al-rich amorphous powder of $Al_{88}Ni_6Ti_6$ composition.[1] The main intention in the present case is to prepare dense and well homogeneous bulk nanocomposites consisting of nanocrystalline intermetallic phases and amorphous phase using different consolidation techniques. The microstructural features and mechanical behaviors of the nanocomposites have been compared and discussed with the help of detailed electron microscopy and nano-indentation.

2. Experimental

Elemental powders of pure (>99.5 wt.%) Al, Ni and Ti having average particle sizes less than 70 μm were mixed under a pro-

* Corresponding author. Tel.: +91 3222 283272; fax: +91 3222 282280.
E-mail address: skpabi@metal.iitkgp.ernet.in (S.K. Pabi).

[1] Composition is expressed in at.%, unless otherwise stated.

0921-5093/$ – see front matter © 2010 Elsevier B.V. All rights reserved.
doi:10.1016/j.msea.2010.03.068

tective atmosphere to obtain a blend of nominal composition $Al_{88}Ni_6Ti_6$. Amorphization of the powder blend was carried out by high energy milling for 120 h in cemented carbide grinding media at a speed of 300 r.p.m. using Fritsch Pulverisette-5 planetary ball mill. The ball to powder weight ratio was 10:1 [26,27] and toluene was used as the process control agent. The phase evolution at different stages of mechanical alloying (MA) was studied by a Philip's X′pert Pro high-resolution X-ray diffractometer using the Co-K_α radiation (λ = 0.178897 nm). The thermal stability of the mechanically alloyed amorphous powder was studied using a differential scanning calorimeter (STA 409C, NETZSCH, Germany) and high temperature X-ray diffraction in vacuum (<1 Pa).

The elemental analysis of the mechanically alloyed amorphous powder was determined by energy dispersive X-ray (EDX) analysis of the sample using a scanning electron microscope (Zeiss, Supra-40), which was fitted with an EDX attachment. The total carbon (C) and oxygen (O) levels in the as-milled powder were determined by elemental analysis using carbon analyzer (LECO, CS-244) and oxygen analyzer (LECO, TC-436), respectively.

The fully amorphous alloy powder was compacted at uniaxial pressure of 1500 MPa and then sintered at 800 °C and 850 °C for 5 h in high purity (impurity level <10 ppm) helium atmosphere by pressure-less sintering. The as-milled amorphous powder was also consolidated by hot-pressing for 20 min at 500 °C at a pressure of 625 MPa. Chrome steel die was used in both the above cases. Besides, the as-milled alloy powder was SPSed at 450 °C and 500 °C for 10 min using a SPS unit (Model 1050, Sumitomo Coal Mining Co. Ltd.) at a pressure of 76.4 MPa in a graphite mold and at 446 MPa in a tungsten carbide (WC) mold. The phase transformation in the sintered specimens was studied by X-ray diffraction (XRD). All the sintered samples were polished with 0.25 μm diamond for metallography, density and hardness measurement. Macroscopic densities of the samples were determined by Archimedes principle using a Sartorius balance with a density measuring kit.

A JEOL JSM-840A scanning electron microscope was used for the microstructural characterization of the powder and the polished sintered specimens. In addition, a field emission scanning electron microscope (Zeiss, Supra-40) was employed to study the microstructural characteristics of the SPSed specimens. A JEOL JEM-2100 transmission electron microscope operating at 200 kV was employed to study the structural features of the as-milled powder and sintered specimens. For transmission electron microscopy (TEM) of the sintered specimens, slices were cut from them by a low speed diamond cutter, and then thinned down to 100 μm by careful grinding. Discs of 3 mm diameter were punched out of the thinned slices by a mechanical punch (Gatan Model 642). The discs were further thinned to ~20 μm by means of a dimpler (Gatan Model-656) and finally thinned to electron transparency by ion milling (Gatan Precision Polishing System Model 691).

Nano-indentation of the sintered specimens was carried out in MTS-XP nanoindenter at a constant load of 50 mN. Average of all the data over the depth of penetration between 100 and 200 nm has been taken as a single data. Each data of the hardness and elastic modulus is a statistical mean of 40 indentations on each specimen. The corresponding standard deviations are also reported. A Leica 550 MW tester was employed for microhardness measurements of the sintered specimens using 5 g load as per the ASTM E92-82 specification. The indenter speed and dwell time were 25 μm s^{-1} and 15 s, respectively.

3. Results and discussion

Fig. 1 shows the XRD patterns of $Al_{88}Ni_6Ti_6$ composition milled for 120 h in comparison with that of the without milled sample, and the hump in the XRD pattern of 120 h milled sample indicates that the complete amorphization was achieved after 120 h of

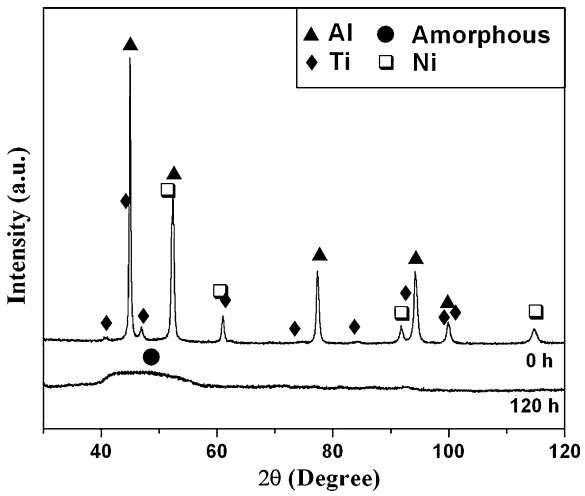

Fig. 1. XRD patterns of $Al_{88}Ni_6Ti_6$ without milling and after 120 h of MA showing phase evolution due to high energy ball milling.

milling. Complete amorphization of this milled powder was further ascertained from the diffused halo in the corresponding electron diffraction (ED) pattern, as shown in the inset of the bright field TEM image of the 120 h milled powder (Fig. 2). Moreover, the TEM image of 120 h milled powder in Fig. 2 indicated that the amorphous powder was agglomerated and had nano-features. Complete amorphization of the $Al_{88}Ni_6Ti_6$ composition by MA was reported earlier by Das et al. [26,27].

It is known that a small amount of impurities can trigger amorphization during ball milling [28,29]. Hence, it is of interest to know the levels of contamination in the present composition at the end of 120 h of ball milling. Therefore, energy dispersive X-ray (EDX) analysis and elemental analysis of the 120 milled powder were carried out. The EDX analysis of the 120 h milled amorphous powder revealed 78.2 wt.% Al, 11.41 wt.% Ni, 8.93 wt.% Ti, which is close to the initial blend composition (i.e.,78.78 wt.% Al, 11.68 wt.% Ni, 9.54 wt.% Ti). The remaining 1.46 wt.% possibly contains oxygen in the form of oxides and other impurities like carbon, etc. contaminated from the milling media. The elemental analysis of the

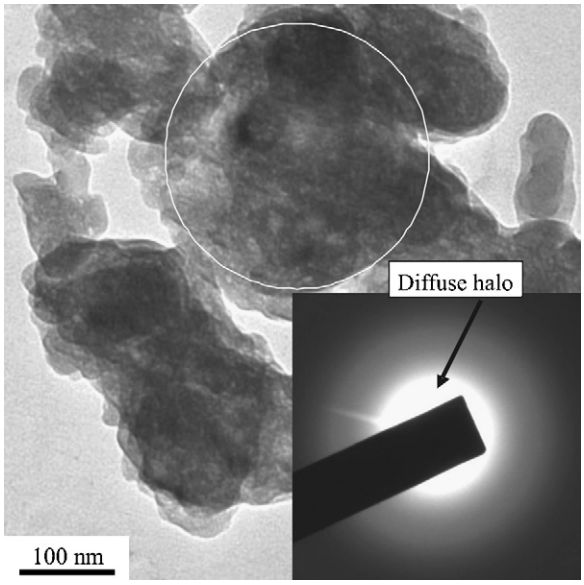

Fig. 2. TEM micrograph of $Al_{88}Ni_6Ti_6$ after 120 h of MA. The ED pattern (in the inset) from the encircled area of the micrograph shows the diffused halo indicating complete amorphization of the composition after 120 h of MA.

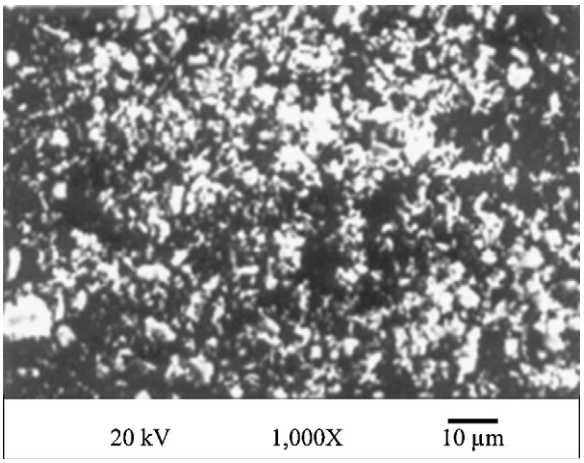

Fig. 3. SEM micrograph of $Al_{88}Ni_6Ti_6$ composition after MA for 120 h showing sub-micron sized particles seemed to be agglomerated.

amorphous powder showed the presence of C ~0.33 wt.% and O ~0.48 wt.% as contaminations in the powder after MA for 120 h. These impurity contaminations might have provoked the amorphous phase formation of the present composition by ball milling.

The scanning electron microscopy (SEM) of the ball-milled $Al_{88}Ni_6Ti_6$ powder revealed gradual refinement of the powder particles with the progress of MA. After 15 h of MA, the powder product showed a layered non-uniform structure. Upon further milling, the different constituent elements of the powder blend are no longer distinguishable by SEM, and the sub-micron sized particles seem to be agglomerated, as shown in Fig. 3.

Fig. 4a shows the DSC trace of the amorphous nanostructured powder of $Al_{88}Ni_6Ti_6$ composition studied by DSC under flowing argon atmosphere. During DSC temperature was raised up to 1200 °C and heating rate was 5 °C/min. The material initially underwent possibly a glass transition, which is indicated by an endothermic trend [30] at ~476 °C (Fig. 4a) with increasing temperature, and this is possibly the glass transition temperature, T_g, for the present amorphous powder. During further heating, first exothermic transformation corresponding to crystallization from the glass was observed at ~520 °C, and this is possibly the first crystallization temperature, T_x, of $Al_{88}Ni_6Ti_6$ amorphous powder. Thereafter, several prominent exothermic peaks appeared at different temperatures, which were indicative of some phase transformation in the milled glassy structure as indicated in Fig. 4a. Finally, a large endothermic transformation was seen at ~1020 °C (T_M), as indicated in Fig. 4a, representing the melting of the crystalline phases. A magnified view of the DSC trace around the T_g and T_x is shown in Fig. 4b to obtain clear features around T_g and T_x.

In order to get an insight into this event, the amorphous powder was analyzed by XRD, carried out at different temperatures and is presented in Fig. 4c. The amorphous structure seems to be quite stable up to 250 °C, since no significant changes are observed in the XRD patterns at temperatures up to 250 °C, as indicated in Fig. 4c. The XRD pattern at 400 °C shows peaks corresponding to a number of intermetallic phases, namely, Al_2Ti, Ni_4Ti_3, $NiTi_2$, $AlTi_3$ and Al_3Ni_2, superimposed on the amorphous hump. It is very difficult to calculate the crystallite size of these compounds from the peak broadening because of weak intensity. The XRD profile at 550 °C revealed some extra crystalline peaks due to formation of phases, namely, Ni_3Ti, $AlNi_3$, and Ni_5Al_3 along with those phases formed at 400 °C. The presence of Al peaks in the XRD pattern of the powder at 550 °C indicates the formation of Al particles in the amorphous matrix along with the formation of intermetallic phases. The amorphous hump in the XRD patterns of the as-milled powder gradually

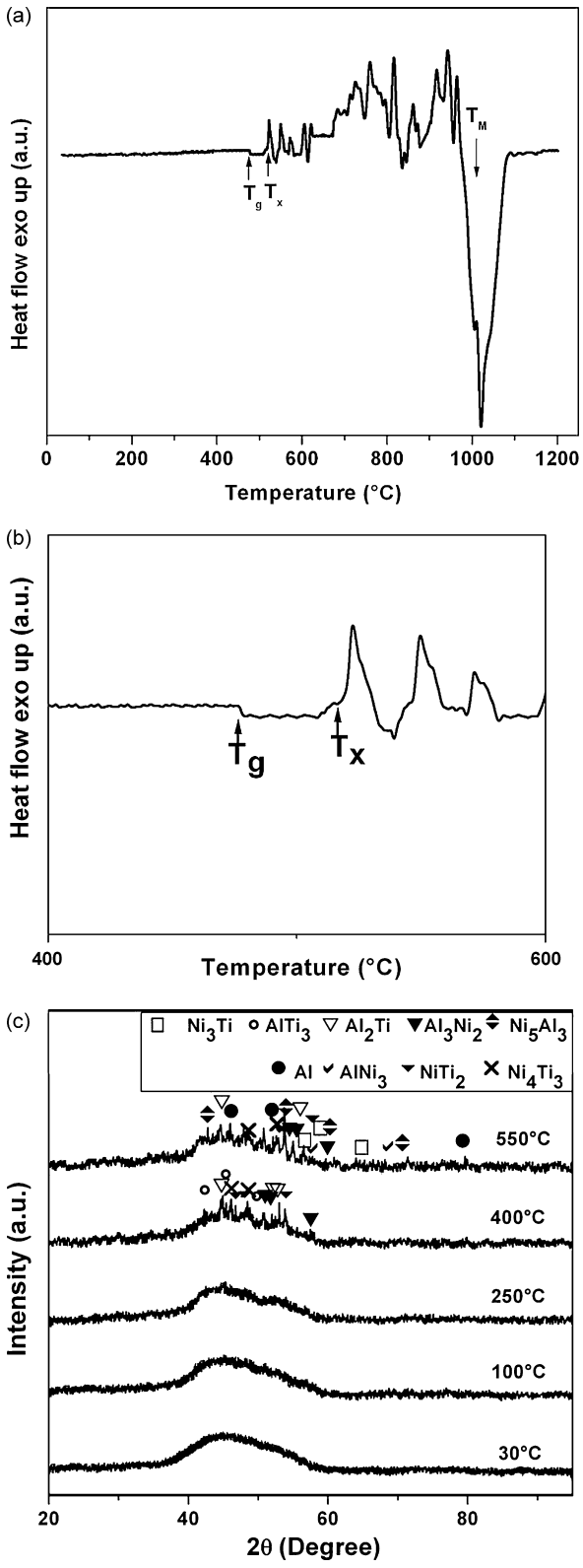

Fig. 4. (a) DSC trace showing glass transformation (T_g), devitrification (T_x) and melting (T_M) of a $Al_{88}Ni_6Ti_6$ amorphous powder. Data recorded during heating at a rate of 5 °C/min under flowing argon atmosphere (impurity level <10 ppm). (b) Magnified view of the DSC trace around T_g and T_x showing the features around T_g and T_x. (c) XRD profiles of the amorphous powder of $Al_{88}Ni_6Ti_6$ recorded at different temperatures demonstrating the formation of different phases.

Table 1
Sintered density, percentage densification, temperature, applied pressure and duration of loading for the corresponding sintering methods.

Sintering method	Pressure and time	Temperature and die used	Sintered density (kg m^{-3})	Densification[a] (%)
Pressure-less sintering	0 MPa and 5 h	850 °C and Cr Steel	2423	86.2
Hot-pressing	625 MPa and 20 min	500 °C and Cr Steel	2462	87.6
SPS	76.4 MPa and 10 min	450 °C and Graphite	1939	68.9
SPS	76.4 MPa and 10 min	500 °C and Graphite	1971	70.1
SPS	446 MPa and 10 min	450 °C and Tungsten carbide	2603	92.6
SPS	446 MPa and 10 min	500 °C and Tungsten carbide	2694	95.8

[a] Relative to the density of amorphous powder, 2811 kg m^{-3}.

disappears with the increase in temperature above 250 °C, and it is concurrent with the formation of intermetallic compounds.

It seems that the thermal stability of the present alloy is better than that of the alloy having similar composition $Al_{85}Ni_{10}Ti_5$ [31]. It has also been reported that T_x of $Al_{95-x}Ni_xTi_5$ gradually decreases as atomic fraction of Ni decrease with a consequence increase in Al content. T_x of $Al_{85}Ni_{10}Ti_5$ is about 300 °C. Interestingly, the present $Al_{88}Ni_6Ti_6$ alloy has much higher T_x (520 °C). Higher crystallization temperature implies higher thermal stability of the amorphous phase. However, the present alloy is made by ball milling whereas the alloys reported by Kim et al. [31] are made by melt spinning. Though the present alloy composition is falling close to the mixture of crystalline and amorphous line in the ternary diagram [31], it may be possible that high energy ball milling could extend the composition range for the formation of amorphous phase. Moreover, T_x of the amorphous alloy is strongly dependent on the composition [5]. The slight variation of the composition may play an important role in determining the crystallization temperature of amorphous alloy [5]. In the present alloy, a slight higher amount of Ti is possibly responsible for its higher thermal stability, presumably due to the much lower diffusivity of Ti [5]. The DSC data and XRD patterns in Fig. 4a–c indicated that the consolidation of the mechanically alloyed amorphous powder below 550 °C within a short duration through an appropriate consolidation method can potentially generate a nanocomposite consisting of nano-sized intermetallic phase(s) dispersed in the amorphous matrix [19]. It is known that the mechanical properties of the amorphous matrix composite can be quite attractive, as compared to that of the conventional composite materials [19].

The amorphous powder was sintered using different methods, viz., conventional pressure-less sintering, hot-pressing and spark plasma sintering with a view to producing bulk samples for the evaluation of their mechanical properties and to characterize the related microstructural features. Table 1 summarizes the percentage densification obtained by different sintering methods at different applied pressures and temperatures. Pressure-less sintering at 850 °C for 5 h under helium atmosphere resulted in ~86% densification, whereas hot-pressing for 20 min at an applied pressure of 625 MPa led to a similar level of densification (~87.6%). Both the above techniques use chrome steel as the die material. On the other hand, SPS carried out at 450 °C and 500 °C for 10 min at a pressure of 76.4 MPa in graphite mold shows density of ~70%. Hence, densification in graphite die does not show significant densification by the SPS under specified pressure and temperature. However, samples made by SPS at a pressure of 446 MPa in WC die at 450 °C and 500 °C for 10 min show a remarkable improvement in the sintered density of the order of 92% and ~96%, respectively. It is attributed to the use of WC die which permitted the application of much higher pressure compared to graphite die.

Fig. 5 shows the XRD patterns of the samples sintered by three different techniques at different temperatures and pressures. Conventional pressure-less sintering at 800 °C leads to the formation of different intermetallic phases, namely, Al_3Ti, Al_5Ti_3, Ni_4Ti_3 and AlNi. Sintering at 800 °C by pressure-less consolidation does not result in equilibrium phases, since the equilibrium phases in the present alloy at 800 °C are Al_3Ni, Al_3Ti and liquid Al [32]. New crystalline phases such as Al_3Ni, Al_3Ni_2 and Ti_6O form along with the elemental Ni if temperature is raised to 850 °C (Fig. 5). In addition, the amorphous hump in the XRD profile has completely disappeared indicating the formation of a predominantly crystalline structure after sintering at temperatures ≥800 °C. Higher temperatures are warranted in case of pressure-less sintering in order to achieve better densification, and the absence of Al peak in the sintered product at 800 or 850 °C suggests possible interference from these high melting intermetallic phases towards the formation of equilibrium phases. The need to sinter at temperatures 800 or 850 °C, which are well above the melting temperature of pure Al, essentially points out that the crystalline components in the sintered products are predominantly of high melting intermetallics and these intermetallic phases were formed possibly well before reaching the melting point of pure Al. On the other hand, XRD patterns of the compact obtained by hot-pressing at 500 °C at a pressure of 625 MPa for 20 min shows the formation of a few intermetallic compounds comprising of only Al and Ti, viz., Al_5Ti_3 and Al_3Ti along with an amorphous phase which is evident from the amorphous shallow hump (Fig. 5). However, the lower sintered density of the order 87.6% of these hot pressed pellets (Table 1) is not sufficient for possible structural applicability.

XRD patterns of the samples prepared by SPS at 450 °C and 500 °C for 10 min at an applied pressure of 446 MPa in WC die show the formation of Al_3Ni, Ni_4Ti_3, $AlTi_3$, $Al_{0.30}Ni_{0.35}Ti_{0.35}$ intermetallic phases (Fig. 5). The presence of a significant amorphous hump of the samples prepared by SPS technique indicates the possibility of forming composite containing an amorphous phase. In general, the increase in relative peak intensities of the crystalline phases

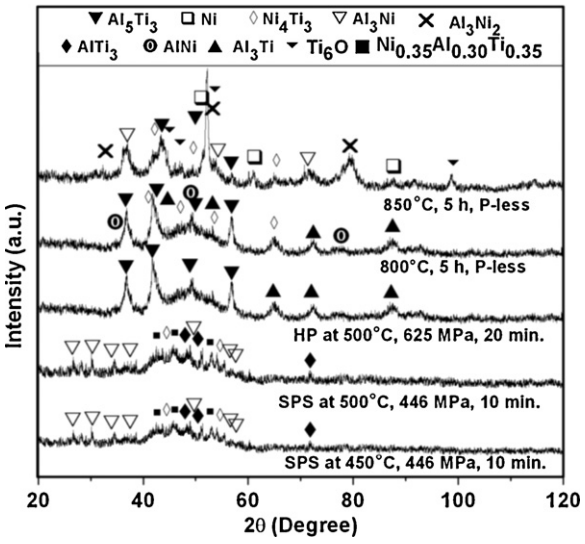

Fig. 5. XRD profiles of initially amorphous $Al_{88}Ni_6Ti_6$ sintered by pressure-less (P-less), hot-pressing (HP) and SPS method indicating the phase evolution after consolidation.

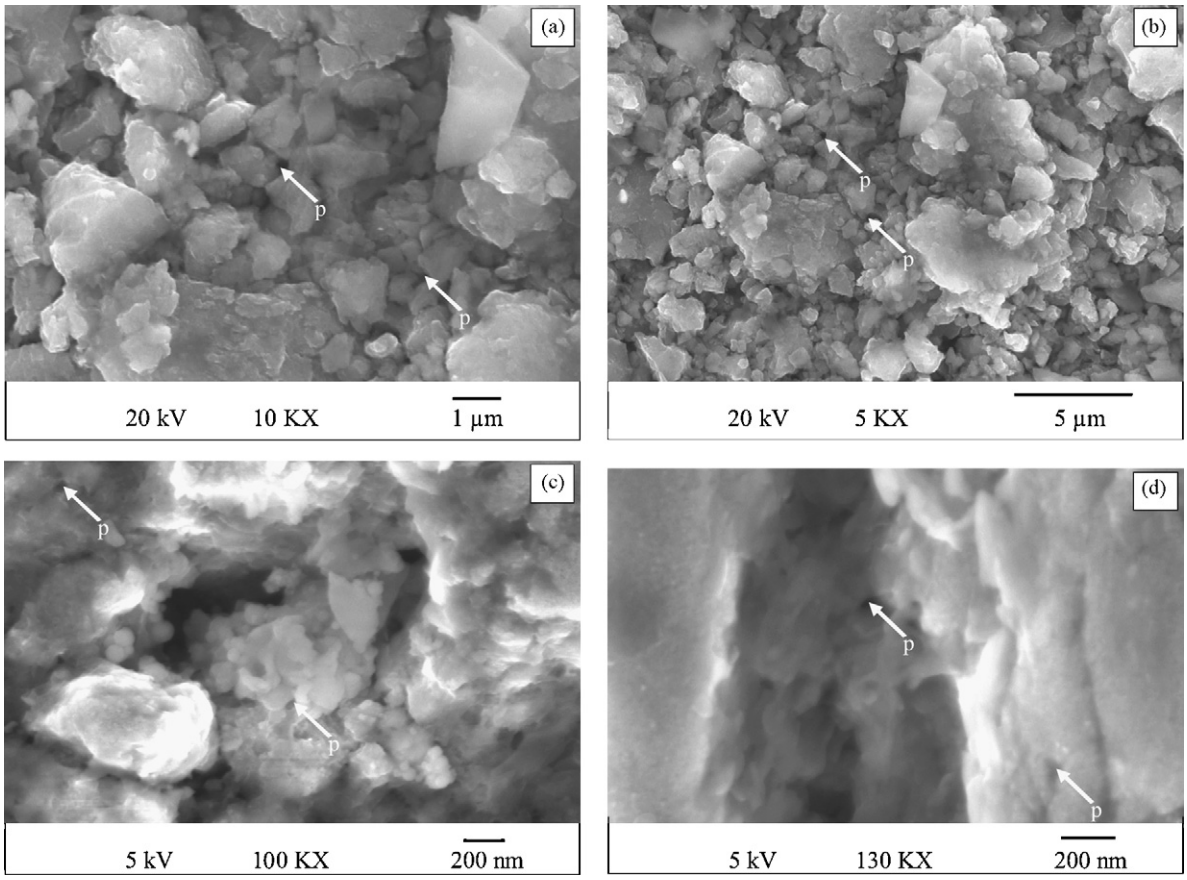

Fig. 6. SEM micrographs of (a) conventionally sintered at 850 °C, (b) hot pressed at 500 °C for 20 min at a pressure of 625 MPa and SPSed at (c) 450 °C, (d) 500 °C under the applied pressure of 446 MPa for 10 min specimens showing the nature of microstructure (P on the microstructures indicates porosity).

indicates an increase in the crystallinity of the specimen with the increase in the temperature and duration of sintering.

Fig. 6a–d displays the SEM micrographs of the sintered samples consolidated by different methods. The conventional sintering at 850 °C shows considerable presence of intergranular porosity with a mixture of coarse and finer particles ranging from ≤1 to 5 μm (Fig. 6a). The sample hot pressed at 500 °C shows a larger proportion of fine particles (Fig. 6b) compared to the former cases. The microstructure of the sample SPSed at 450 °C at an applied pressure of 446 MPa (Fig. 6c) clearly shows much finer grain size (<1 μm) and little porosity as compared to those shown in Fig. 6a and b. In contrast, when the SPS temperature was raised to 500 °C, a highly densified structure has been obtained (Fig. 6d). The microstructure of the sample SPSed at 450 °C under an applied pressure of 446 MPa (Fig. 6c) clearly shows finer grain size (<1 μm) compared to those shown in Fig. 6a and b, but the product is not free from pores indicating partial densification at 450 °C. In contrast, when the SPS temperature was raised to 500 °C, a highly densified structure was obtained and the fracture was no longer intergranular (Fig. 6d). The SEM micrographs of the sintered specimens in Fig. 6 are in good agreement with the experimentally measured values of macroscopic densities of the specimens reported in Table 1.

The SEM images in Fig. 6a–d were recorded on the polished surfaces of the sintered specimens at magnifications of 5–130k×. Limited bonding between the particles during pressure-less sintering and hot-pressing is evident from the low densification (densification ~87%). This effect gets reflected in the SEM micrographs (Fig. 6a and b) also. SEM micrographs from SPSed samples (Fig. 6c and d) were taken at a magnification of 100k× and 130k×, respectively. Hence, the very high magnification enables to reveal the features of the individual particles too.

The bright field TEM image and corresponding selected area diffraction (SAD) pattern in the inset in Fig. 7a of the sample prepared by pressure-less sintering at 850 °C result in a predominantly crystalline structure, which is in good agreement with the corresponding XRD pattern in Fig. 5. Fig. 7b shows the presence of a diffuse halo in the SAD pattern of the hot pressed specimen indicating the presence of an amorphous phase. The presence of fine rings in the SAD pattern is attributed to the presence of nanocrystalline intermetallics. Hence, the microstructure is typically a distribution of an amorphous phase and nanocrystalline intermetallic phases. Fig. 7c shows the dark field TEM image of the specimen SPSed at 500 °C at an applied pressure of 446 MPa in WC die. It is clear that there is a uniform dispersion of the nanocrystalline phases of size less than 20 nm. The ring patterns and diffuse halo in the SAD pattern in Fig. 7c suggest the presence of nanocrystalline intermetallic precipitates along with the amorphous phase. Recently, Das et al. [33] also have shown the presence of nanocrystalline phases in the amorphous matrix by high-resolution TEM imaging.

The accelerated densification mechanisms involved during the consolidation of the amorphous/nanocrystalline materials by SPS technique are not yet well understood [20]. The interparticle electric discharge and current effect may play role for the fast sintering in the SPS method [34,35]. For an electrically conductive specimen (as in the case of the present alloy), uniform heating and enhanced mass transport can result due to the pulsed current (Joule effect) and the heat transfer from the die and punches [34,36]. Since the conductivity of WC at room temperature (~63 $W m^{-1} K^{-1}$) [37] is similar to that of graphite (63–210 $W m^{-1} K^{-1}$) [38], both the die would lead to uniform temperature distribution in the compressed sample. Koizumi et al. [39] explained the role of applied pressure in the SPS as quasi-isostatic, i.e., isostatic in the inner region of the

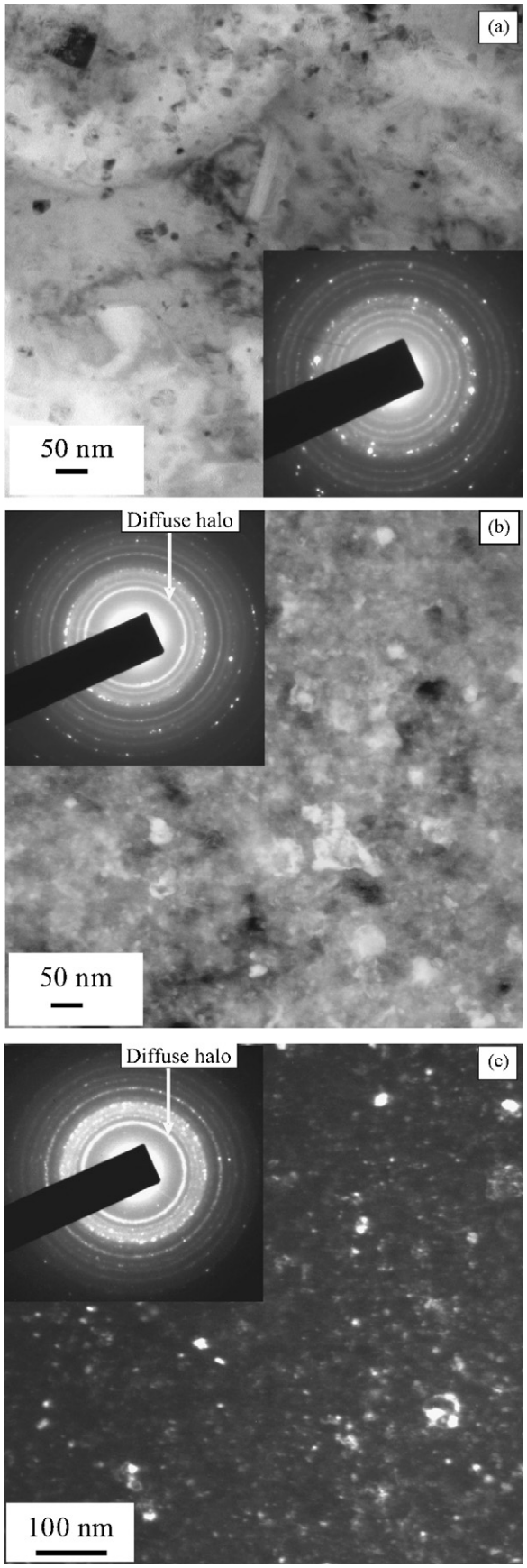

Fig. 7. TEM micrographs and corresponding ED patterns of the sintered compacts of $Al_{88}Ni_6Ti_6$ showing particle size and nature of crystallinity of the consolidated specimens: (a) conventionally sintered at 850 °C, (b) hot pressed at 500 °C and (c) SPSed at 500 °C.

compact and non-isostatic near the surface region. However, the ultrafine powder produced by MA normally has a granular shape, and it may be possible to apply isostatic pressure to most of the regions of the specimen, because the granular powders may serve as the pressure-transmitting medium in the SPS process [40]. In general, it is believed that the pulsed current promotes the removal of adsorbents or surface oxides due to plasma generation [41], and thereby enhances the bonding of the particles. Further densification of the nanostructured powders may be accomplished by several mechanisms such as plastic deformation, grain boundary sliding [42], grain growth and grain rotation [43] and even by grain boundary melting [44]. Recent molecular dynamics simulation of the consolidation of amorphous nano-particles has revealed that the nano-sized cavities in the green compacts can get filled up very rapidly within a fraction of second during sintering due to the high diffusivity of atoms in the glassy phase [45]. Probably spherical shape of the MA powder and much higher pressure can enhance the above processes leading to much better densification when WC is used as the die material in comparison to graphite die.

Table 2 shows the elastic modulus and hardness obtained from nano-indentation and microhardness of the conventionally sintered (at 850 °C), hot pressed (at 500 °C, 625 MPa) and SPSed (at 450 °C and 500 °C, 446 MPa) samples. The elastic modulus of the hot pressed specimen was marginally higher (~2%) than that of the conventionally sintered specimen. The elastic modulus of the specimens produced by the SPS treatment at 450 °C and 500 °C were ~5.5% and ~9.5% higher, respectively, than that of the conventionally sintered specimen. The elastic modulus of the metals and alloys is not sensitive to the structural features like grain size, point defects, dislocation density, etc. [46]. Therefore, the marginally higher elastic modulus of the SPSed specimens must have originated from its higher sintered density (Table 1). It is also interesting to note from Table 2, that the standard deviation in the values of elastic modulus is much higher in the case of conventionally sintered or hot pressed specimens compared to that of the SPSed samples, which seems to be due to inhomogeneous sintering in the former two cases (Table 1).

Sample consolidated by conventional pressure-less sintering technique at 850 °C shows a nano-indentation hardness of 5.18 GPa and microhardness of 4.8 GPa. It is likely that the sample consolidated at 850 °C by pressure-less sintering has mostly crystallized as observed from the XRD patterns (Fig. 5) and corresponding SAD pattern (Fig. 7a). However, samples consolidated by hot-pressing and SPS have considerable fraction of amorphous phase along with the nanocrystalline intermetallic phases as interpreted from the amorphous hump of the XRD patters of these samples (Fig. 5) and amorphous halo observed in SAD patterns (Fig. 7b and c). However, SPSed sample is likely to have larger fraction amorphous phase because of much lower sintering temperature in comparison to that prepared by hot-pressing. Hence, it can be concluded that the samples prepared by SPS technique are truly nanocomposite with a microstructure of nanocrystalline phases dispersed in an amorphous matrix. Nano-indentation hardness values of the samples prepared by hot-pressing and SPS are ~25% and 40–64% more than that of the sample prepared by pressure-less sintering, respectively (Table 2). Average microhardness values of the samples consolidated by the above sintering techniques follow the same trend (Table 2). Therefore, the hardness and density of the samples consolidated by different sintering techniques have good proportionality as observed from Tables 1 and 2.

The maximum microhardness of around 7.9 GPa obtained in the present Al-based amorphous + nanocrystal nanocomposite sample consolidated by SPS in WC die at 500 °C for 10 min is much higher than that reported for other Al-rich nanocomposites with similar microstructures [19,47,48]. Schurack et al. [47] reported a Vickers

Table 2
Elastic modulus and hardness of specimens produced by conventional pressure-less sintering at 850 °C, hot-pressing at 500 °C, and SPS at 450 °C and 500 °C.

		Pressure-less sintering at 850 °C	Hot-pressing at 500 °C	SPS at 450 °C	SPS at 500 °C
Nano-indentation test	Elastic modulus Y (GPa)	69.5 ± 4.1	70.9 ± 3.2	73.3 ± 1.9	76.2 ± 1.6
	Nano-indentation hardness (GPa)	5.18 ± 0.10	6.46 ± 0.08	7.24 ± 0.03	8.51 ± 0.01
	Microhardness (GPa)	4.8	5.9	6.7	7.9

microhardness of ~4.2 GPa[2] in the mechanically alloyed and consolidated $Al_{85}Y_8Ni_5Co_2$ alloy, and the fracture strength of the same was estimated to be ~1.4 GPa. Dougherty et al. [48] reported even higher microhardness values of 6.1–6.4 GPa for the mechanically alloyed and subsequently consolidated $Al_{80}Ni_8Fe_4Gd_8$ alloy, and the corresponding fracture strength was estimated to be ~2 GPa. This high strength was attributed to the presence of additional intermetallic precipitates and/or oxides in the material [19]. The maximum microhardness of ~7.9 GPa obtained in the present amorphous based nanocomposite is much higher than the values reported for other amorphous based Al-rich nanocomposites [19]. Apparently, the high volume fraction of glassy matrix (which normally has a high yield strength of ~900 MPa in Al alloys [19]), better densification, as well as, the homogeneous distribution of nano-sized precipitates in the amorphous matrix, obtained by SPS of the present amorphous powder, seem to be responsible for its superior mechanical properties. This high strength is definitely attributed to the highly dense and uniform distribution of a large number of additional intermetallic fine precipitates. Highest nano-indentation hardness obtained from a sample consolidated by SPS at 500 °C for 10 min in WC die (~8.51 GPa) is close that of the hot compacted fcc-Al-based nanocomposite of Al-TM (TM = Ti, Zr, Fe) alloy containing nano-sized dispersion of $L1_2$-Al_3(Ti,Zr) intermetallics (~8.6 GPa) [49].

4. Conclusions

Three different consolidation techniques have been tried to make high strength Al-based nanocomposite with a microstructure of fine and uniform distribution of nanocrystalline intermetallic phases in amorphous matrix. SPS technique in WC die has been found out to be most effective in getting highest densification and best strength level in the consolidated samples compared to pressure-less and hot-pressing. The maximum hardness of the order of 8.51 GPa of the consolidated Al-based amorphous + nanocrystal composite prepared by SPS is compared well to even fully nanocrystalline Al-based composite. Higher fraction of amorphous content, finer and uniform distribution of nanocrystalline intermetallic phase in amorphous matrix are the possible reason for best densification and highest strength for the SPSed samples compared to other two methods.

Acknowledgement

The authors highly appreciate the Department of Science and Technology, Govt. of India (grant no. SR/S5/NM-91/2002) for financial support.

References

[1] A. Inoue, Nanostruct. Mater. 6 (1995) 53–64.
[2] C. Suryanarayana, E. Ivanov, V.V. Boldyrev, Mater. Sci. Eng. A 304–306 (2001) 151–158.
[3] C.S. Kiminami, N.D. Basim, M.J. Kaufman, M.F. Amateau, T.J. Eden, G.J. Galbraith, Key Eng. Mater. 89 (2001) 503–508.
[4] T. Masumoto, Mater. Sci. Eng. A 179–180 (1994) 8–16.
[5] A. Inoue, Prog. Mater. Sci. 43 (1998) 365–520.
[6] H. Gleiter, Acta Mater. 48 (2000) 1–29.
[7] C.C. Koch, Nanostruct. Mater. 9 (1997) 13–22.
[8] K. Lu, Mater. Sci. Eng. R 16 (1996) 161–221.
[9] J. Xu, G.S. Collins, L.S.J. Peng, M. Atzmon, Acta Mater. 47 (1999) 1241–1253.
[10] M.S. El-Eskandarany, M. Matsushita, A. Inoue, J. Alloys Compd. 329 (2001) 239–252.
[11] M.K. Datta, S.K. Pabi, B.S. Murty, J. Appl. Phys. 87 (2000) 8393–8400.
[12] F. Wu, P. Bellon, A.J. Melmed, T. Lusby, Acta Mater. 49 (2001) 453–461.
[13] F. Cardellini, G. Mazzone, M.V. Antisari, Acta Mater. 44 (1996) 1511–1517.
[14] J. Latuch, T. Kulik, H. Dimitrov, Mater. Sci. Eng. A 375–377 (2004) 956–960.
[15] P. Ramchandra Rao, Z. Metallkd. 71 (1980) 172–177.
[16] T. Egami, Mater. Sci. Eng. A 226–228 (1997) 261–267.
[17] T.T. Sasaki, K. Hono, J. Vierke, M. Wollgarten, J. Banhart, Mater. Sci. Eng. A 490 (2008) 343–350.
[18] Y. Li, Y.H. Zhao, V. Ortalan, W. Liu, Z.H. Zhang, R.G. Vogt, N.D. Browning, E.J. Lavernia, J.M. Schoenung, Mater. Sci. Eng. A 527 (2009) 305–316.
[19] J. Eckert, in: C.C. Koch (Ed.), Nanostructured Materials-Processing, Properties and Potential Applications, Noyes, New York, 2002, pp. 423–525.
[20] J.R. Groza, in: C.C. Koch (Ed.), Nanostructured Materials-Processing, Properties and Potential Applications, Noyes, New York, 2002, pp. 115–178.
[21] J.R. Weertman, in: C.C. Koch (Ed.), Nanostructured Materials-Processing, Properties and Potential Applications, Noyes, New York, 2002, pp. 397–421.
[22] B.Q. Han, J. Ye, F. Tang, J.M. Schoenung, E.J. Lavernia, J. Mater. Sci. 42 (2007) 1660–1672.
[23] Y.S. Park, K.H. Chung, N.J. Kim, E.J. Lavernia, Mater. Sci. Eng. A 374 (2004) 211–226.
[24] R. Chaim, Z. Shen, M. Nygren, J. Mater. Res. 19 (2004) 2527–2531.
[25] W. Jo, T.-H. Kim, D.-Y. Kim, S.K. Pabi, J. Appl. Phys. 102 (2007), 074116 (1–8).
[26] N. Das, G.K. Dey, B.S. Murty, S.K. Pabi, Pramana—J. Phys. 65 (2005) 831–840.
[27] N. Das, M. Tech. Thesis, IIT Kharagpur, 2005.
[28] Y.Y. Li, C. Yang, W.P. Chen, X.Q. Li, M. Zhu, J. Mater. Res. 22 (2007) 1927–1932.
[29] J. Balogh, L. Bujdoso, T. Kemeny, I. Vincze, J. Phys.: Condens. Matter 9 (1997) L503–L508.
[30] R.F. Speyer, Thermal Analysis of Materials, vol. 42, Marcel Dekker, Inc, NY, 1994, pp. 35–42, 183–184.
[31] D.H. Kim, W.T. Kim, D.H. Kim, Mater. Sci. Eng. A 385 (2004) 44–53.
[32] J.R. Davis (Ed.), Aluminum and Aluminum Alloys, ASM Specialty Handbook, ASM International, The Materials Information Society, USA, 1998, p. 573.
[33] J. Das, M.B. Tang, K.B. Kim, R. Theissmann, F. Baier, W.H. Wang, J. Eckert, Phys. Rev. Lett. 94 (2005), 205501 (1–4).
[34] V. Mamedov, Powder Metall. 45 (2002) 322–325.
[35] J. Ye, L. Ajdelsztajn, J.M. Schoenung, Metall. Mater. Trans. A 37A (2006) 2569–2579.
[36] M. Omori, Mater. Sci. Eng. A 287 (2000) 183–188.
[37] Hugh O. Pierson, Handbook Of Refractory Carbides & Nitrides: Properties, Characteristics, Processing And Apps, Noyes publication, USA, New Jersey, 1996, pp. 1–340.
[38] E.A. Brandes, G.B. Brook (Eds.), Smithells Metals Reference Book, seventh ed., Butterworth-Heinemann, Oxford, 1992, pp. 27–33.
[39] Y. Koizumi, T. Tanaka, Y. Minamino, N. Tsuji, K. Mizuuchi, Y. Ohkanda, Mater. Trans. 44 (2003) 1604–1612.
[40] E.A. Olevsky, E.R. Strutt, M.A. Meyers, J. Mater. Process. Technol. 121 (2002) 157–166.
[41] T.J. Goodwin, S.H. Yoo, P. Matteazzi, J.R. Groza, Nanostruct. Mater. 8 (1997) 559–566.
[42] G.E. Fougere, J.R. Weertman, R.W. Siegel, Nanostruct. Mater. 5 (1995) 127–134.
[43] R.S. Averback, H. Zhu, R. Tao, H.J. Hofler, in: D.L. Bourell (Ed.), Synthesis and Processing of Nanocrystalline Powder, TMS, Warrendale, PA, 1996, pp. 203–216.
[44] H. Zhu, R.S. Averback, Mater. Manufact. Proc. 11 (1996) 905–923.
[45] D. Sopu, A. Stuko, S. Ghosh, K. Albe, H. Gleiter, Unpublished work.
[46] G.E. Dieter, Mechanical Metallurgy, SI Metric Edition, McGraw Hill Book Company, London, U.K, 1988, 280-281.
[47] F. Schurack, I. Borner, J. Eckert, L. Schultz, Mater. Sci. Forum 312 (1999) 49–54.
[48] G.M. Dougherty, G.J. Shiflet, S.J. Poon, Acta Metall. Mater. 42 (1994) 2275–2283.
[49] S.S. Nayak, Ph.D. thesis, IIT Kharagpur, 2008.

[2] http://www.gordonengland.co.uk/hardness/hvconv.htm.